

FORKLENS: Accurate weak lensing shear measurement on extremely noisy images with deep learning

Zekang Zhang^{1,2*}, Huanyuan Shan^{1,2**}, Nan Li³, Chengliang Wei⁴, Ji Yao¹, Ran Li^{3,5,6}

¹ Shanghai Astronomical Observatory, Chinese Academy of Sciences, Shanghai 200030, PR China

² University of Chinese Academy of Sciences, Beijing 100049, PR China

³ National Astronomical Observatories, Chinese Academy of Sciences, Beijing 100101, PR China

⁴ Purple Mountain Observatory, Chinese Academy of Sciences, Nanjing, 210023, PR China

⁵ Institute for Frontiers in Astronomy and Astrophysics, Beijing Normal University, Beijing 102206, China

⁶ School of Astronomy and Space Science, University of Chinese Academy of Science, Beijing 100049, China

January 10, 2023

ABSTRACT

Context. Weak gravitational lensing is one of the most important probes of the nature of dark matter and dark energy. In order to extract cosmological information from next-generation weak lensing surveys (e.g., *Euclid*, *Roman*, LSST, and CSST) as much as possible, accurate measurements of weak lensing shear are required.

Aims. There are existing algorithms to measure the weak lensing shear on imaging data, which have been successfully applied in previous surveys. In the meantime, machine learning has been widely recognized in various Astrophysics applications in modelling and observations. In this work, we present a fully deep-learning-based approach to measuring weak lensing shear accurately.

Methods. Our approach comprises two modules. The first one contains a CNN with two branches for taking galaxy images and PSF simultaneously, and the output of this module includes the galaxy's magnitude, size, and shape. The second module includes a multiple-layer Neural Network to calibrate weak lensing shear measurements. We name the program FORKLENS and make it publicly available online.

Results. Applying FORKLENS to CSST-like mock images, we achieve consistent accuracy with traditional approaches (such as moment-based measurement and forward model fitting) on the sources with high signal-to-noise ratios (S/N). For the sources with meagre S/N, FORKLENS exhibits powerful latent denoising ability and offers accurate predictions on galaxy shapes.

Conclusions. The final shear measurements with FORKLENS deliver a multiplicative bias $m = -0.4 \pm 3.0 \times 10^{-3}$ and an additive bias $c = -0.5 \pm 1.9 \times 10^{-4}$. Our tests with CSST-like simulation show that FORKLENS is competitive with other shear measurement algorithms such as METACALIBRATION, while FORKLENS can potentially lower the S/N limit. Moreover, the whole procedure of FORKLENS is automated and costs about 0.6 milliseconds per galaxy, which is appropriate to adequately take advantage of the sky coverage and depth of the upcoming weak lensing surveys.

Key words. cosmology:observations – gravitational lensing: weak – methods: data analysis

1. Introduction

Gravitational lensing is a phenomenon that describes the deflection of light from background sources by the gravitational potential of matter. It has become one of the most promising tools for the study of various topics in astrophysics, as it is directly sensitive to the distribution of matter, including both dark and visible matter. In the weak lensing regime, the deflection distorts account for only few percents of the object's intrinsic shape, also called 'shear'. By measuring the spatially correlated shears of an ensemble of galaxies, one can map the mass profile of galaxy clusters, identify voids, and even probe the large-scale matter distribution of the Universe. By further considering galaxy redshifts, weak lensing is also used to study the growth of structure and the nature of dark energy (for a recent review on weak gravitational lensing Mandelbaum 2018).

Since the first detection decades ago (Bacon et al. 2000; Kaiser 2000), cosmic shear has matured into an important approach for cosmological surveys. Several large surveys have now been put into action, including the Kilo Degree Survey (KiDS,

Hilbrandt et al. 2017a), the Dark Energy Survey (DES, Krause et al. 2017), and the Subaru Hyper SuprimeCam lensing survey (HSC, Aihara et al. 2018). There are also several upcoming experiments, such as *Euclid* (Laureijs et al. 2011), the Nancy Grace Roman Space Telescope (*Roman*, Spergel et al. 2015), the Large Synoptic Survey Telescope (LSST, LSST Science Collaboration et al. 2009), and the Chinese Space Station Telescope (CSST, Zhan 2011, 2021).

The methods of weak lensing shear measurement are usually tested in simulations mimicking the real observations, where the galaxy images are sheared by a known value \mathbf{g}_{true} . The bias resulted from various systematics between the estimated shear \mathbf{g} and the true signal is conventionally described approximately as a linear model with an additive bias \mathbf{c} and a multiplicative bias \mathbf{M} (Heymans et al. 2006; Massey et al. 2007),

$$\hat{\mathbf{g}} - \mathbf{g}_{\text{true}} = \mathbf{M}\mathbf{g}_{\text{true}} + \mathbf{c} \quad (1)$$

where \mathbf{g} is a two-component vector, and so is \mathbf{c} . \mathbf{M} is a 2×2 matrix, while typically the off-diagonal elements are negligible and the diagonal elements are approximately the same. In this work, we examine our methods on an average of multiplicative

* e-mail: zhangzekang@shao.ac.cn

** e-mail: hyshan@shao.ac.cn

bias m and additive bias c . The requirement for Stage IV weak lensing experiments (e.g., *Euclid*) gives that $|m| \lesssim 2 \times 10^{-3}$ and $|c| \lesssim 2 \times 10^{-4}$ (Massey et al. 2013).

One of the major sources of systematics is the effect of point spread function (PSF) from either the atmosphere or the optical effect of the telescope itself, while pixel response and charge diffusion may also be taken into consideration. PSF smears the shape of observed galaxies and dilutes the shear estimate which causes a multiplicative bias. PSF anisotropy also affects the measured galaxy ellipticity (i.e., PSF leakage), causing an additive bias. This requires careful treatment and correction when inferring precise weak lensing distortion (Paulin-Henriksson et al. 2008, 2009).

For shear measurement, there have traditionally been two approaches: (1) one measures the weighted quadrupole moments of the image light profile (Kaiser et al. 1995; Rhodes et al. 2000; Melchior et al. 2011); (2) one fits the image assuming a galaxy and PSF model (Massey & Refregier 2005; Nakajima & Bernstein 2007; Miller et al. 2013). Both moments-based methods and model-fitting methods can produce quite accurate estimates of galaxies with high signal-to-noise ratio (S/N) but suffer significant "noise bias" which is difficult to predict. The pixel noise can translate into a complicated and skewed distribution of the measured ellipticity (Melchior & Viola 2012), which then propagates into bias in shear estimation. It can be seen as a function of image S/N, galaxy size, shape, and surface brightness, and also the PSF shape if not well corrected. These methods have been well applied in previous surveys where an S/N threshold cut on galaxy samples is introduced. This could lead to further selection bias and lower the galaxy number density when inferring shear correlations. Some of the previous works derived the function of these properties in simulation and apply the calibration to survey data (Miller et al. 2013; Kuijken et al. 2015; Jarvis et al. 2016; Hoekstra et al. 2015). KiDS (Fenech Conti et al. 2017; Hildebrandt et al. 2017b) used the "self-calibration" technique which is directly operated on the measurements instead of simulation. Another wide-recognized new method is METACALIBRATION (Huff & Mandelbaum 2017; Sheldon & Huff 2017), which is based on an early similar idea by Kaiser (2000). METACALIBRATION introduces a tiny artificial shear directly on the observed image and calculates the shear response of the observed galaxy ellipticity. This method has been validated on various simulations and shows good accuracy to a cut at S/N ~ 6 with a specific formalism to deal with selection bias. An updated version named METADETECTION (Sheldon et al. 2020) is further proposed to account for the effect of multi-source blending, although it does not provide a solution for redshift de-blending (MacCrann et al. 2022). There are also some methods able to reach sub-percent level accuracy without calibration using external simulations, for example, Bayesian Fourier Domain (BFD, Bernstein et al. 2016), FOURIER_QUAD (Zhang et al. 2019; Li & Zhang 2021), and Fourier power function shapelets (FPFS, Li et al. 2022; Li & Mandelbaum 2022).

In the meantime, the importance of machine learning (ML) applications in weak lensing measurement has been rapidly recognized over the past decade. Very large ensembles of galaxies across the sky are required for precision cosmology. The resolution and field of view of next-generation surveys have been increasing fast. ML has natural advantages in handling a large amount of data with low CPU and time costs compared to traditional methods such as model fitting. Over the past decade, ML has had wide applications in gravitational lensing, from shear measurement (Neural Network, NN: Gruen et al. 2010; Tewes et al. 2019; Pujol et al. 2020; Hopfield Neural Network, HNN:

Nurbaeva et al. 2015; Convolutional Neural Network, CNN: Ribli et al. 2019a; Springer et al. 2020), convergence map and mass reconstruction (Generative Neural Network, GNN: Shirasaki et al. 2019; U-Net: Jeffrey et al. 2020), lensing modelling and simulation (CNN: Pearson et al. 2019, 2021; GNN: Lanusse et al. 2021), to cosmological constraints (CNN: Fluri et al. 2018; Ribli et al. 2019b; Lu et al. 2022).

CNN has been used to infer shape information directly from images at the pixel level. Ribli et al. (2019a) has developed a 13-layer CNN to measure galaxy shapes and apply it to DES Y1 catalogue, showing better consistency with CFHTLenS shapes. Multi-layer fully-connected NNs have been used to emulate the relation between shear bias and observed galaxy properties. Gruen et al. (2010) first proposed to let neural networks analyze the data and estimate shear after training them on simulations with known shear, using the ellipticity measurement from a specific method (e.g., KSB) and further parameters that might be indicative of the bias calibration (such as galaxy size and magnitude). With similar motivation, Tewes et al. (2019) uses the same network to perform shear estimation in presence of various feature noises like instrument effects, unknown galaxy morphology, and image noise. They took moment-based measurements on individual galaxy's shape as input, including ellipticity, flux, radial extension, and the concentration of the light profile. The network output the shear estimator based on these noisy galaxy features. Instead of minimizing the original mean squared error between target shear and galaxy features, they formulate a mean square bias (MSB) which favours the accuracy in the predictions of the explanatory variables. The training data is then carefully structured so that the NN is able to learn the general relation of the shear estimator to various galaxy realizations. Both two works did not use neural networks on the pixelated light distribution of the galaxy but integrated the NN-based calibration with traditional methods like KSB. A similar idea can also be seen in Pujol et al. (2020), where they use a multi-layer NN to map the relation between the measured image properties of an individual galaxy and the shear bias.

In this work, we propose the FORKLENS method, including a fork-like deep CNN which takes both galaxy and PSF images as input to measure the galaxy's shape and an artificial NN to calibrate the shear bias. Considering the mock images of the CSST survey, we show the accuracy of our CNN on extremely noisy data and its strengths over traditional methods. We organize this paper as follows: we introduce our network architecture and method in Sec. 2; we show our simulations for CSST and our training data organization in Sec. 3; we present our results of shape and shear measurement and compare to traditional methods in Sec. 4; We conclude in Sec. 5.

2. Methodology

FORKLENS is a fully deep-learning-based method which contains two parts. The outline of the architecture is shown in Fig. 1. In the first part, we use a CNN to measure an individual galaxy's shape (together with its size and magnitude) from the pixelated image and simultaneously correct the effect of PSF smearing. Based on the CNN measurement, we then use a NN to estimate the shear response of the galaxy and perform calibration.

2.1. CNN architecture for shape measurement

One of the major challenges in weak lensing analysis is to accurately measure the shapes of small, faint galaxies, which are usually overwhelmed by observational noise. In practice, one can

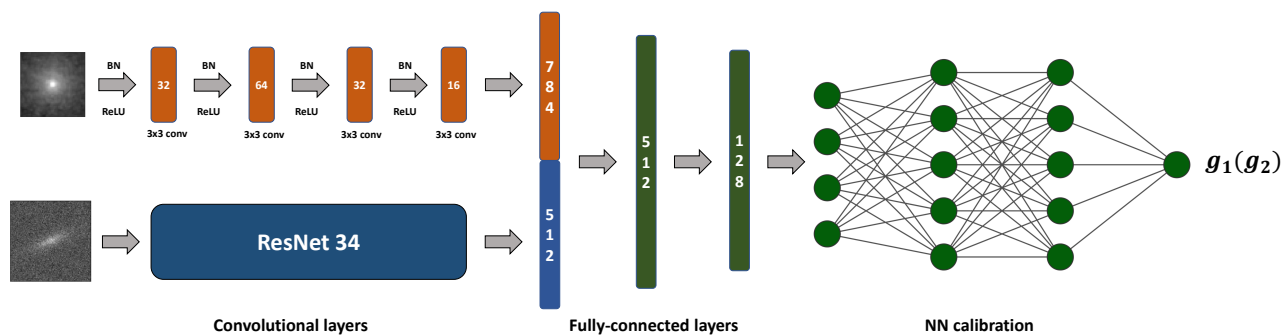


Fig. 1. The outline of FORKLENS shear estimation architecture. The CNN part contains two branches, one fed with PSF and one fed with galaxy image. The PSF branch has four convolutional layers each with batch normalization and ReLU activation function. We adopt a 34-layer residual network, to extract the information of galaxies where the image is larger and suffers from pixel noise. The two branches are then concatenated following two fully-connected layers, where the effect of PSF is corrected. CNN then outputs the galaxy’s properties including size, magnitude, and ellipticities. A further NN calibrates the measured features biased by noise and outputs the final shear estimate. The NN part is in practice a committee of 8 independent NNs and the $g_1(g_2)$ is the average of the 8 outputs.

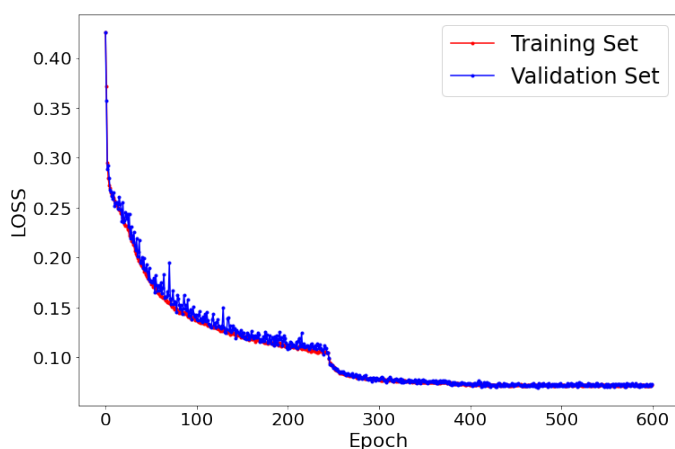


Fig. 2. Training and validation LOSS of CNN. 20,000 pairs of galaxy and PSF are used in total with a 10% validation split and the batch size is 200. The initial learning rate is 0.01 and reduced by 0.1 times when the LOSS (Eq. 2) has stopped improving. We take the model at the 600th epoch as our best one.

never perfectly measure the ellipticities as various noises can undermine the ability to extract the true shape information of the object. Viola et al. (2014) list three origins of measurement bias: 1) model bias when a wrong galaxy model is adopted to describe the observation; 2) bias for the shape measurement algorithm; 3) the bias introduced due to observation noise, which is caused by the non-linearity of galaxy morphology parameters in the image pixels. All methods to measure galaxy shapes are sensitive to noise bias even at a high signal-to-noise ratio. Deep learning (DL) has its natural advantages of identifying noise patterns in the image and retrieving less-biased detection. Although unsupervised learning has been seen in many astrophysics applications, for example, astronomical object identification (Han et al. 2022; Wei et al. 2022), supervised learning is more widely adopted in regression problems. In this case, the trained model may heavily rely on the assumed model used in the simulation and training set. Model bias therefore still requires careful treatment.

We build a custom fork-like CNN architecture with two input paths, one for the observed galaxy (128×128 pixel stamp) and one for the PSF (48×48 pixel stamp). We adopt ResNet34 for

the first path and the second path consists of four convolutional layers, four batch normalization layers, and four layers of Rectified Linear Unit (ReLU) activation function. The final layers of both paths are flattened and concatenated, before being fed into three fully-connected layers. The final layer outputs a four-node array ($n_{\text{fea}} = 4$) which is the predicted properties of the galaxy before PSF convolution (two components of its ellipticity, half light radius of the disk, and the magnitude in i band). The four outputs are then fed into another neural network for unbiased shear estimates.

Deep layers of CNN are believed to progressively learn more complex features. A growing depth has been required for accurate predictions of both image classification (Krizhevsky et al. 2012; Zeiler & Fergus 2014) and regression (?) tasks. However, normal deep networks are generally hard to train and face problems like vanishing/exploding gradient. ResNet (He et al. 2015) is constructed by a series of "residual blocks" which differs from normal layers with a skip connection or a "shortcut". Such a shortcut directly adds the input of a block to its output, which enables to train much deeper networks than what was previously impossible. ResNet34 consists of 16 residual blocks with 34 convolutional layers in total and our results see no improvement in adopting deeper ResNet.

To train the CNN, we input a minibatch size of $n_{\text{bat}} = 200$ for 600 complete iterations on the whole train set, namely 600 epochs. We use stochastic gradient descent (SGD) as the parameter optimizer. The learning rate is initially set as 0.1 and is reduced by a magnitude when the metric has stopped improving. We adopt the mean squared error between each element in the input labels x and the predicted outputs y as our LOSS function,

$$\text{LOSS} = \frac{1}{n_{\text{bat}}} \sum_{i=1}^{n_{\text{bat}}} \frac{1}{n_{\text{fea}}} \sum_{n=1}^{n_{\text{fea}}} (x_{n,i} - y_{n,i})^2 \quad (2)$$

which is averaged over elements every minibatch. In this work, we do not use any hyperparameter optimization to tune the CNN architecture. Fig. 2 shows the training and validation LOSS. We make FORKLENS publicly available¹.

In order to evaluate the performance of the fork-like CNN architecture, we also run other well-tested methods on the same data including moments-based measurement and model fitting to make comparisons.

¹ <https://github.com/zhangzzk/forklens>

For shapes based on moments, we use the EstimateShear function in the HSM module of *GalSim* software package² (Rowe et al. 2015). There are several algorithms included in the function re-implemented from different works (e.g., 'BJ' by Bernstein & Jarvis 2002, 'LINEAR' and 'REGAUSS' by Hirata & Seljak 2003). We find their performances are quite similar and we adopt the 'REGAUSS' option throughout this paper.

For model fitting, we employ the route implemented in *Ngmix* software package³ (Sheldon 2015). The galaxy is fitted to a single Gaussian convolved by another single Gaussian representing the PSF. *Ngmix* provides other more complicated models with multiple Gaussians. Yet no apparent improvement is seen adopting these models and the speed is much slower with more free parameters to fit. Following Zuntz et al. (2018), we adopt flat priors on all model parameters except the prior on ellipticity, which is the isotropic unlensed distribution as the Eq. 24 in Bernstein & Armstrong (2014) with $\sigma = 0.1$.

2.2. NNs architecture for shear calibration

In common with other existing methods, the CNN ellipticity measurements are biased by pixel noise. A noisy measurement of image ellipticity e can be expanded in a Taylor series about shear \mathbf{g} ,

$$\mathbf{e} = \mathbf{e}|_{\mathbf{g}=0} + \frac{\partial \mathbf{e}}{\partial \mathbf{g}}|_{\mathbf{g}=0} \mathbf{g} + \dots, \quad (3)$$

where the first-order term is called the shear response,

$$\mathbf{R} = \frac{\partial \mathbf{e}}{\partial \mathbf{g}}|_{\mathbf{g}=0}, \quad (4)$$

and the zero-order will be statistically cancelled out over an ensemble of galaxies assuming their intrinsic shapes are randomly oriented. METACALIBRATION derives the response \mathbf{R} by applying an artificial shear to observed images and calculating the changes in the measurement of e (we will give more details in Sec. 4.3).

In this work, we follow the same formula from Tewes et al. (2019) to perform shear calibration, but instead, take the measurement of our CNN as input. Four values are fed into the neural network (including two components of ellipticities, galaxy half light radius, and apparent magnitude), which are further passed into two hidden layers of five nodes each and output the estimator of g_1 (g_2). Activation functions in all input and hidden nodes are the hyperbolic tangent $f(x) = \tanh(x)$. In the output layer, it is an identity activation function. All inputs are normalized in an interval $[-1, 1]$.

The network is optimized by minimizing the MSB loss function with a Broyden-Fletcher-Goldfarb-Shanno (BFGS) iterative optimization algorithm,

$$\text{MSB}(\mathbf{f}) = \frac{1}{n_{\text{case}}} \sum_{i=1}^{n_{\text{case}}} \left[\frac{1}{n_{\text{rea}}} \sum_{j=1}^{n_{\text{rea}}} \hat{g}_{ij}(\mathbf{f}) - g_i^{\text{true}} \right]^2 \quad (5)$$

where \mathbf{f} denotes the input galaxy features.

The network parameters are initialized randomly from a normal distribution, and different initialization will lead to different shear estimate outputs. To exploit this stochastic behaviour, a committee of eight identical but independent NNs is trained with the same data. The final shear estimate is the average over the

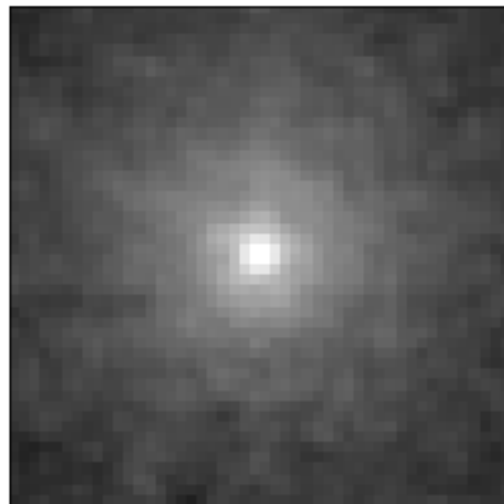
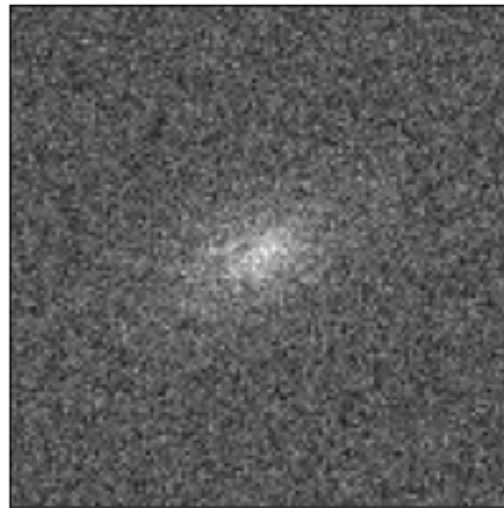


Fig. 3. CSST simulation of an example galaxy (top, half light radius of 1.2 arcsecs, 20 in magnitude, $e_1 = 0.4$ and $e_2 = -0.4$) and PSF in log scale (bottom, drawn from random positions on the CCD in simulation). Both shot noise and Gaussian noise are included in the observed galaxy. PSF is simulated based on the optical design model (Sec. 3.1).

outputs of the best four NN members (according to their training loss). In this part of shear calibration training, we use the public-available code *tenbilac*⁴ from Tewes et al. (2019).

In Tewes et al. (2019), they exclude the galaxies with $S/N < 10$ when training the shear estimator described above, as KSB is not able to provide reliable measurements or even fails to detect extremely faint images. But they do include these galaxies in the following analysis, which leads to higher bias in both m and c . To solve the problem, they further introduce a similar network to predict the weight of different galaxies according to their properties (mainly S/N). By down-weighting the shear estimates of faint galaxies, the overall accuracy of shear measurement on an ensemble of various galaxies can be significantly improved. Similar operations have been seen in previous surveys (e.g., Miller et al. 2013; Fenech Conti et al. 2017), where the weight on each

² <https://github.com/GalSim-developers/GalSim>

³ <https://github.com/esheldon/ngmix>

⁴ <http://cdsarc.u-strasbg.fr/viz-bin/qcat?J/A+A/621/A36>

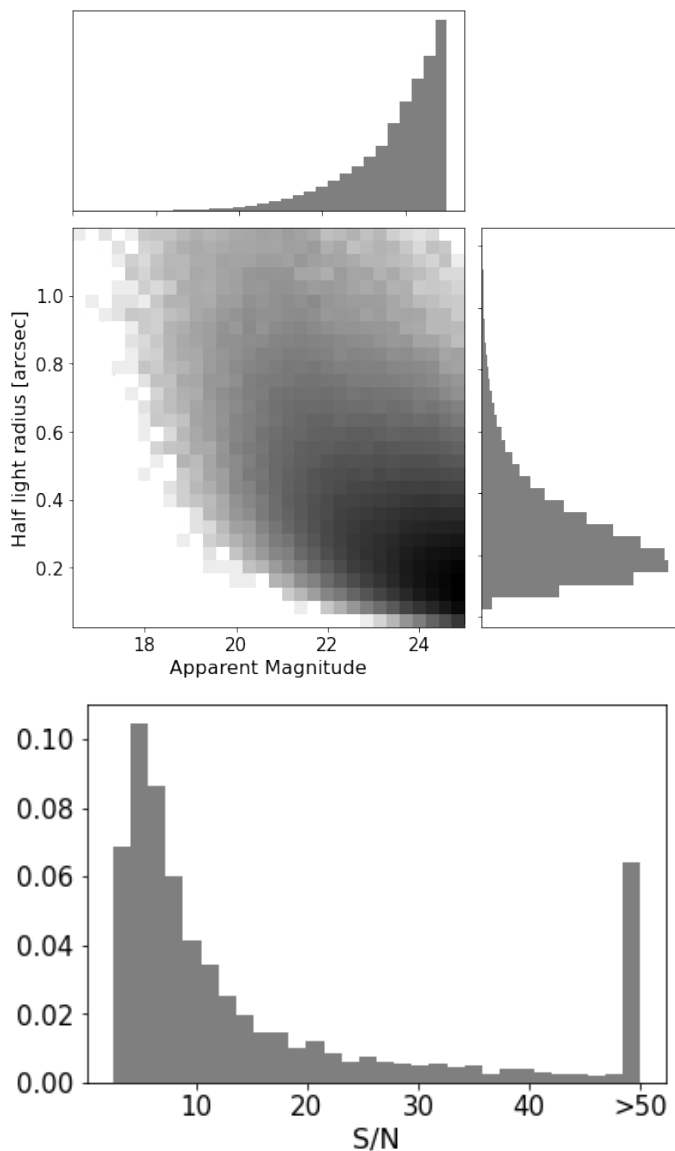


Fig. 4. Distribution of the simulated CSST galaxies, from which we randomly draw for training and testing sets (with different random seeds). Top: Distributions of galaxy half light radii and magnitude. Bottom: Normalized distribution of galaxy signal-to-noise ratio. Galaxies with $S/N > 50$ sit in the bin ~ 50 .

galaxy’s ellipticity measurement is a function of the shape noise variance and the measurement variance. In this work, we will show later that we would not require weighting as CNN can provide tight estimates for very noisy images. We acknowledge that there will be a potential improvement in the overall accuracy if adopting weighting, especially when various systematics are considered such as model bias or complicated noise patterns.

3. Datasets

3.1. CSST imaging simulations

All the data in this work is generated with the CSST simulation code, where the imaging part is based on *Galsim*. CSST simulation contains an end-to-end pipeline from numerical cosmology simulation and gravitational ray tracing to optical instruments and imaging. Various instrumental effects are taken into consideration as on/off options, including cosmic ray, brighter-fatter

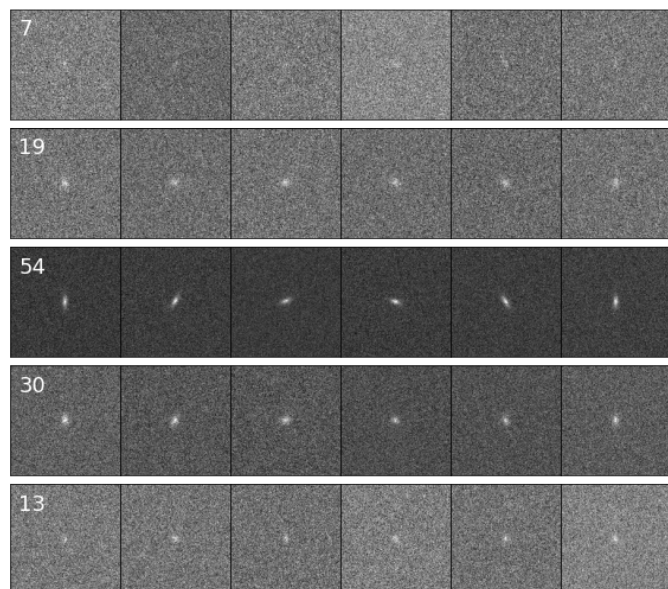


Fig. 5. The structured data set to train the calibration NN with the MSB loss function (similar to Fig. 2 in Tewes et al. 2019). Each row corresponds to one case containing 2000 galaxies (i.e., 2000 columns), which differ only in the orientations sharing the same shear and PSF. 5000 cases (i.e., 5000 rows) in total are used to train the NN. Shape noise cancellation is adopted.

effect, charge diffusion effect, non-linear, CTI effect and etc. We do not include these effects in our simulations and plan to dig into their impact on our weak lensing measurement and cosmological constraints in future works.

The galaxy includes an exponential disk, convolved with non-stationary PSFs simulated for CSST (an example is shown in Fig. 3). We generate galaxies stamp with a size of 128×128 pixels, with pixel size 0.074 arcsec. We assume a perfectly known PSF on a stamp of 48×48 pixels put into the network. The distribution of galaxy parameters (magnitude, galaxy half light radius, signal-to-noise ratio) is shown in Fig. 4. We only consider single-band measurement in this work, although Ribli et al. (2019a) shows a slight improvement in accuracy with multi-band images.

Instead of parametric models, the PSF is derived based on an optical design model. To generate a set of realistic PSFs to account for the impact of the optical system on image quality, an optical emulator has been developed to simulate high-fidelity PSFs of CSST. The optical emulator of CSST is based on six different modules to simulate the optical aberration due to mirror surface roughness, fabrication errors, CCD assembly errors, gravitational distortions, and thermal distortions. Moreover, two dynamical errors, due to micro-vibrations and image stabilization, are also included in the simulated PSF.

3.2. Data organization

Galaxy properties including magnitude and half light radius used in training and analysis are drawn from the CSST catalogue, shown in Fig. 4. Galaxy orientation and axis ratio are drawn from uniform distributions. Different PSFs at random positions on the CCD are arbitrarily assigned to each galaxy and assumed to be perfectly known when performing measurements. We use a data set of 20,000 galaxy and PSF pairs in total to train the CNN. 2000 pairs are used for validation, to make sure the model is

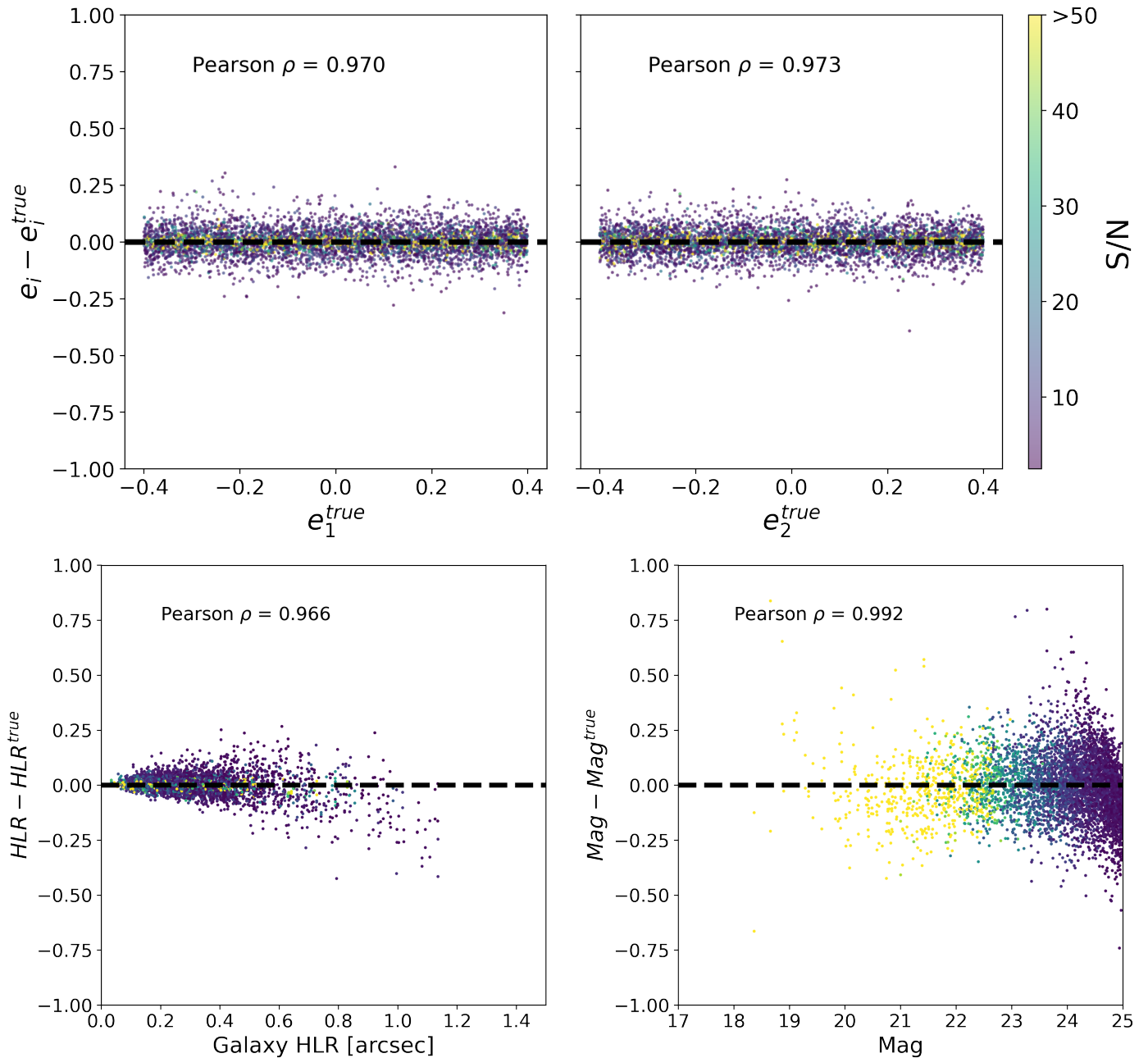


Fig. 6. Overview of the shape measurement residuals on 5000 galaxies of CSST simulations, including ellipticities (top), galaxy half light radius (HLR, bottom left), and magnitude in *i* band (bottom right). Colours denote the signal-to-noise ratio of images and those with $S/N > 50$ are shown as the same colour as 50. The measurement of all four features is generally tight. We notice relatively higher residuals in HLR measurements for large yet very faint galaxies, the size of which is underestimated. Nevertheless, the number is small and its effect on ellipticity measurement is negligible.

not overfitting and is generally valid for data not involved in the optimization.

To train the NNs, we follow the data structure adopted by Tewes et al. (2019), in which data are catalogued into "cases" and "realizations" (see Fig. 5). A realization is a single observation including a galaxy and its PSF. A case is an ensemble of realizations for the same value of a known shear. The training data is grouped into 5000 cases of different magnitudes, galaxy sizes, PSF, and applied shear. Inside each case, there are 2000 realizations sharing the same galaxy and PSF properties (including galaxy axis ratio), and a known shear, but varying in the galaxy orientations. Here in each case, we adopt the "intrinsic shape

cancellation" technique, which makes sure the galaxies are perfectly randomly oriented and there is no "shape noise" residuals left averaging their intrinsic ellipticities. More specifically, half of the galaxies are derived by simply rotating 90 degrees of the other and we then have 1000 pairs of orthogonal galaxies inside each case. Among cases, the shear randomly varies from -0.1 to 0.1, and galaxy properties are again sampled from the CSST mock catalogue. Different PSFs are also randomly assigned to each case.

For a given size of the galaxy (e.g., 1.2 arcsecs of half light radius), the galaxy profile will fall outside the edge of our 128×128 stamp cut with too large ellipticity. For a non-zero e_1 and

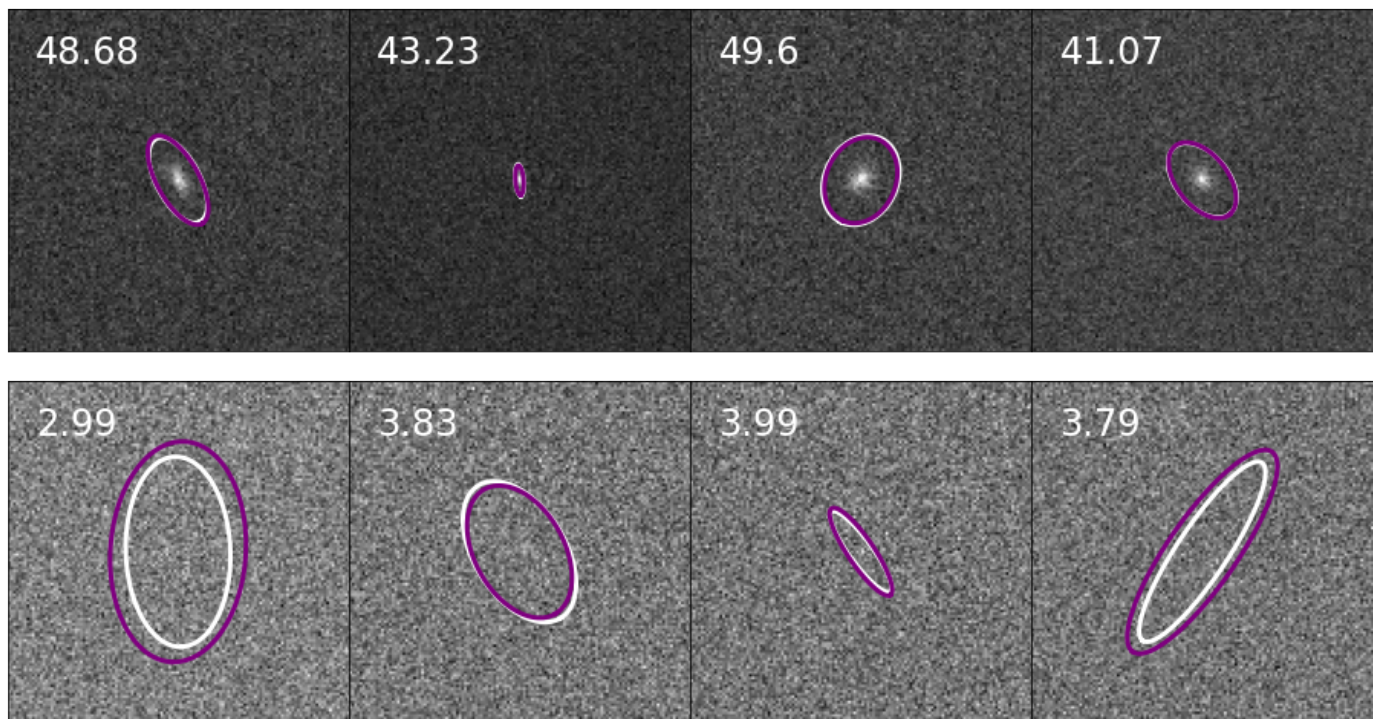


Fig. 7. Galaxy shape measurements after PSF correction for eight example galaxies each with the S/N labelled. The estimates of intrinsic ellipticity and disk half light radius are shown as ellipses of which the sizes are increased by 6 times for illustration purposes. The white ellipses are ground true and the predicted results by CNN are shown in purple.

zero e_2 , we require the galaxy 95% light radius to be smaller than the stamp length of 128 pixels, which translates to $e_1 \lesssim 0.5$ for a pixel scale of 0.074 arcsecs. Considering further shearing with a maximum amplitude of 0.1, we, therefore, cut our ellipticity range at 0.4 for both $|e_1|$ and $|e_2|$, which can be simply expanded by increasing the stamp size.

4. Results

In this section, we show the results of the shear estimation with CSST imaging simulation using FORKLENS. First, we present the results of testing the CNN on CSST simulation, comparing its performance with the moment-based method and model fitting. We then show the shear calibration with NNs based on the outputs of CNN as against the results of METACALIBRATION.

4.1. Feature measurement on CSST simulation

Our definition of signal-to-noise ratio is equivalent to the one used by Great3 (Mandelbaum et al. 2014),

$$(S/N)^2 = \frac{\sum I(x, y)^2}{\text{Var}(I(x, y))} \quad (6)$$

$I(x, y)$ is the noise-free image of galaxy. In simulation, the pixel noise variance $\text{Var}(I(x, y))$ is calculated from the noise map by subtracting the observed image from the noise-free galaxy.

To evaluate the dispersion of shape measurements, we adopt the Pearson correlation coefficient as our metric (Ribli et al. 2019a),

$$\rho(x, y) = \frac{\sigma_{x,y}}{\sigma_x \sigma_y} \quad (7)$$

where $\sigma_{x,y}$ is the covariance of ground truth and predicted results. σ_x and σ_y is the standard deviation respectively. We leave the estimation of multiplicative and additive bias of shear measurement in Sec. 4.2.

We show the overall performance of the CNN predicting four galaxy features in Fig. 6. The accuracy is impressive considering the large fraction of faint galaxies in our simulation. The Pearson coefficients reach ~ 0.97 for ellipticity and size measurement and ~ 0.99 for magnitude measurement. The top panel of Fig. 6 suggests a noticeable dependence of accuracy on galaxy S/N. Bright galaxies have a smaller dispersion than faint ones. For disk size estimation, the dispersion remains nearly constant for different disk HLR when the S/N is high, while it sees a slightly larger dispersion and also a bias for faint disks with half light radius larger than 0.8 arcsecs. The galaxy magnitude shows a clear relation with S/N because of the constant noise level and the measurement is generally accurate.

In real weak lensing surveys, the statistic shear estimation often faces a measurement threshold, for example, a cut on S/N. A large fraction of galaxies fail to be measured when being fitted to a forward model or calculating adaptive moments due to their low S/N or small size. These galaxies with highly biased shape estimates or simply no measurements are excluded by the clean sample (for example, of DES), which may cause a loss of information and "selection bias" (Fenech Conti et al. 2017).

Our CNN shows a strong ability to detect extremely noisy images when galaxy S/N is lower than 10 and even 5. In Fig. 7, we inspect several random examples of how well the CNN can recover the intrinsic shapes of extremely faint images. The predicted shape matches well with true input for both high ($40 < S/N < 50$) and low ($S/N < 5$) S/N bins. It sees an accurate recovery of the galaxy's true shape even when the galaxy

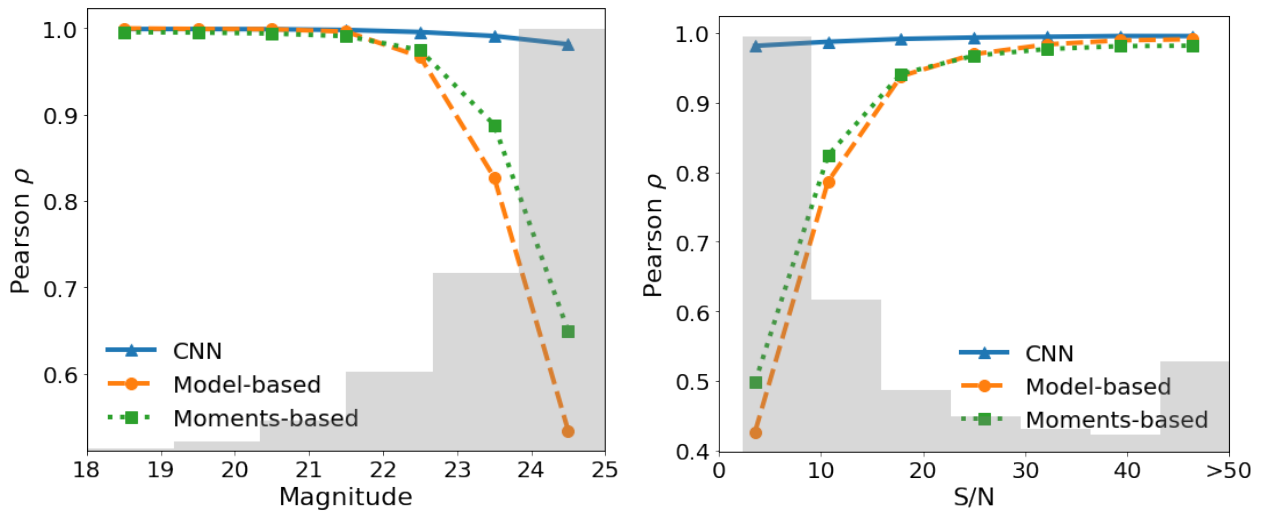


Fig. 8. Pearson coefficient of shape measurements with three methods (CNN; REGAUSS, Rowe et al. 2015; model fitting, Sheldon 2015) as a function of magnitude and galaxy S/N. Grey histograms show the galaxy distributions. Galaxies with S/N > 50 sit in the bin of 45-50. The three methods show consistent accuracy for bright galaxies with high S/N. The accuracy persists for CNN in very faint and noisy images.

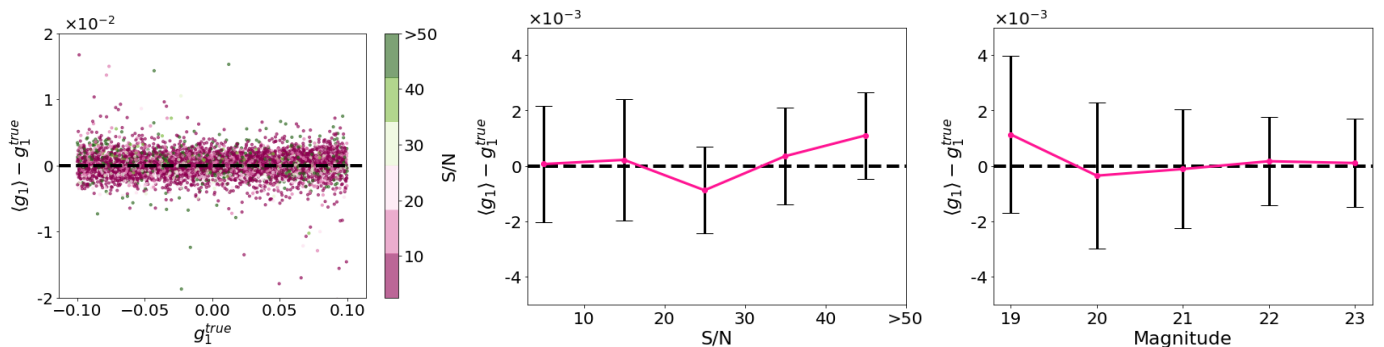


Fig. 9. Left: The shear estimation on data described in Fig. 5 after NN calibration. Each point is one "case" with 2000 "realizations" sharing the same axis ratio, size, magnitude, PSF, and shear but differing in orientation. Right: Binned shear residuals as a function of galaxy S/N. We notice a dependence of residuals on S/N where noisy sources are measured less accurately. Similar dependence can also be seen for galaxy magnitude. Shear measurement is tighter for brighter galaxies.

is overwhelmed by noise. The detection limit reaches down to $S/N \sim 3$ with reliable estimates.

Fig. 8 compares the Pearson coefficient ρ among three methods according to the galaxy magnitude M_i and signal-to-noise ratio. 50,000 galaxies are equally binned into seven groups. In each bin ρ is calculated with the predicted ellipticities by each method and the true labels. For the model- and moments-based methods, the tendency of ρ is similar and is comparable to that of CNN measuring the brightest galaxies. It remains nearly unit at $M_i < 20$ but decreases quickly to ~ 0.5 when $M_i > 24$ and S/N drops to 10 and below. Meanwhile, ρ for CNN stays at ~ 1 and sees only a slight drop in the bin of $M_i \sim 25$ and $S/N < 10$. CNN shows dominant strengths where the image noise begins to overwhelm signals.

4.2. Shear calibration with neural network

We input the four features measured by CNN into a neural network with two hidden layers of five nodes. Information on the PSF would not be necessary since the CNN show good results to preprocess this effect.

We present the overall results of $\langle g_1 \rangle$ estimation training the NN in Fig. 9. We are not showing the results for $\langle g_2 \rangle$ as they

show similar behaviour. We include all S/N ranging down to 2 and over 50% of the images are under 10. NN succeeds in predicting accurate estimates for all galaxies and shear. We notice the estimate is sometimes slightly underestimated at large true shears (i.e., a little lower at $g_1^{\text{true}} \sim 0.1$ and higher at $g_1^{\text{true}} \sim -0.1$). Although this behaviour can increase m , their fraction is small and we do not see a significant effect on the final shear measurement (Fig. 10). On the right of Fig. 9, we also see a weak dependence of shear estimates on galaxy S/N. Very noisy images have slightly worse measurements, as we can expect. This also means an improvement of overall accuracy can be made if further adopting weights on shear estimates according to S/N (also magnitude, size like in Tewes et al. 2019).

In Fig. 10, we present the main results of this work, overall shear measurement on CSST simulation. On the left panel is the direct output of CNN, each data point is the averaged e_1 measurements of 10,000 galaxies drawn from Fig. 4 applying the same shear. Inside each point, we also adopt "shape noise cancellation", where half of the galaxies have the same axis ratio as the other half but the orientation is rotated by 90 degree. By that the averaged intrinsic shape will cancel out to zero. Without this technique, the scattering of the points will be larger since shape noise is included although it will not significantly affect

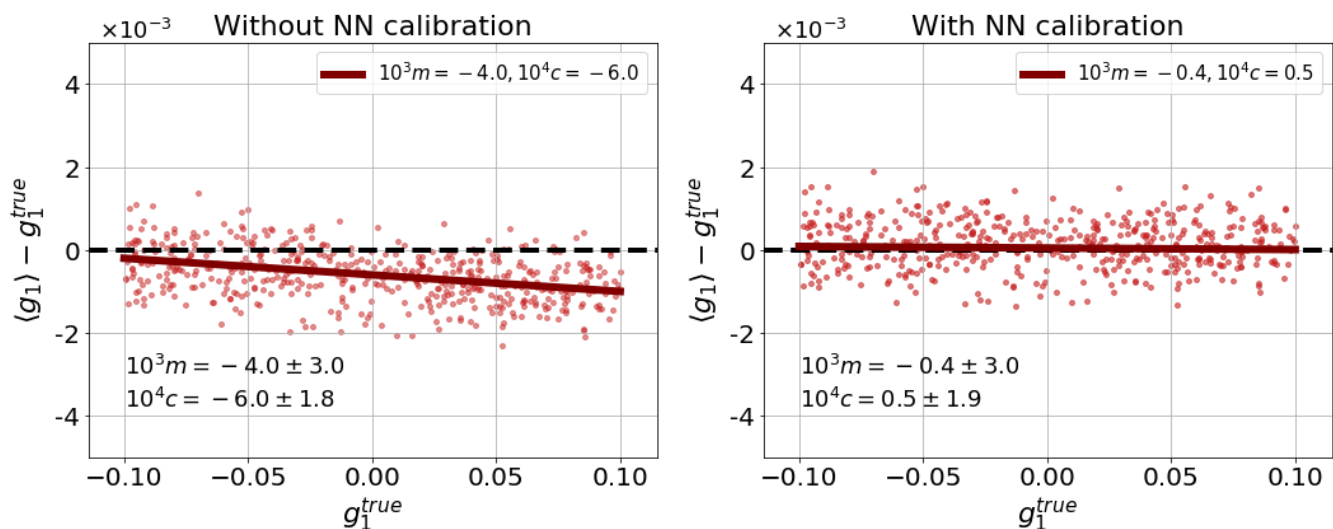


Fig. 10. Final results of shear measurement for CSST with our FORKLENS approach. The left panel is the direct output of CNN and the right is after the calibration with NN. Each point in the plot contains 10,000 varying galaxy and PSF pairs, sharing the same shear. Shape noise cancellation is adopted. There are 50 million image pairs in total in the first panel and the second panel uses the exact same data. Note here no S/N cut or weight is introduced.

the m and c . The measurement from CNN is already good with $m = -4.0 \pm 3.0 \times 10^{-3}$ and $c = -6.0 \pm 1.8 \times 10^{-4}$. We notice the $g_1^{\text{true}} = 0.1$ end is biased while the $g_1^{\text{true}} = -0.1$ end is accurate. A neural network can well calibrate this bias, with corrected $m = -0.4 \pm 3.0 \times 10^{-3}$ and $c = -0.5 \pm 1.9 \times 10^{-4}$ both improved by a magnitude.

4.3. METACALIBRATION on CSST simulation

METACALIBRATION operates directly on observed images, with artificial shearing via a series of image manipulations. In Fourier space, the process can be clearly described as:

$$\tilde{I}(\mathbf{g}) = [(\tilde{I}/\tilde{P} \oplus \mathbf{g})] \times \tilde{P}_d \quad (8)$$

The original galaxy \tilde{I} is deconvolved by its PSF \tilde{P} , sheared by an applied shear \mathbf{g} (in the range of 0.001 to 0.05 and usually 0.01), and reconvolved by a slightly larger PSF than the original one to suppress the amplified noise due to deconvolution.

The response of measured ellipticity to shear can then be derived as,

$$R_{i,j} = \frac{e_i^+ - e_i^-}{\Delta g_j} \quad (9)$$

where e^+ (e^-) is the measured ellipticity of component i ($i = 1, 2$) of an image sheared by $+g_j$ ($-g_j$), and $\Delta g_j = 2g_j$. j denotes the two components of shear.

The calibrated shear estimation is then a weighted average as,

$$\langle \mathbf{g} \rangle \simeq \langle \mathbf{R} \rangle^{-1} \langle \mathbf{e} \rangle \quad (10)$$

where \mathbf{e} is the measured ellipticities on the original galaxy. (For more details please refer to Sheldon & Huff 2017).

This technique has been well tested in the simulation of several surveys and shows a great improvement in shear estimation after calibration (e.g., Yamamoto et al. 2022; Guinot et al. 2022). Not relying on any specific method, METACALIBRATION has the potential and flexibility to be applied to any shape measurement

algorithm. Although METACALIBRATION can account for the effect of PSF without any prior PSF correction, it may be beneficial to adopt some pre-processions in the case of variable PSFs.

Our CNN can also be directly integrated with METACALIBRATION. Ribli et al. (2019a) combined their CNN with METACALIBRATION and find negligible m and c on DES simulations. Since we have used a NN to perform the calibration, we will leave this option in future works and stick to a full-ML approach in this paper. However, we do intend to dig into how our method compares with "METACALIBRATION + model fitting" on the same data, and see if the strength still stands on noisy images.

Fig. 11 is the results of METACALIBRATION together with model fitting. We again use the package NGMIX which provides modules for both METACALIBRATION and model fitting. We fit the images with a single Gaussian convolved with a Gaussian PSF. We run this procedure and our CNN+NN (labelled as "Metacal" and "Forklens" respectively in Fig. 11) approach on the same data, which are 100 cases of different shears each containing 10,000 galaxies (again here we adopt shape noise cancellation). The "Metacal" method requires an S/N cut as forward model fitting fails to provide reliable estimates on shapes of very noisy galaxies (The same goes for the moment-based method). We show the measurement bias as a function of the minimum S/N in the data compared between METACALIBRATION and FORKLENS. We see much higher RMS of "Metacal" measurements as the large error bars indicate, which decreases with higher minimum S/N. This also corresponds to the limitation of shape measurements from model fitting on noisy images. FORKLENS shows a stable bias of both m and c which remains nearly constant for varying S/N cuts. The measurement of CNN is much tighter, although a weak S/N dependence can be seen (similar to Fig. 9). NN succeeds in calibrating the CNN bias to a negligible level, but slightly over-lifts c above zero.

In general, our DL-based approach FORKLENS shows good potential and strength for stage IV surveys. However, we want to stress that the above comparison is not fair competition. Firstly, we do not include multi-components in the galaxy profile. We do not consider complicated morphology for sources at higher redshifts. We leave further comparisons with more complex sce-

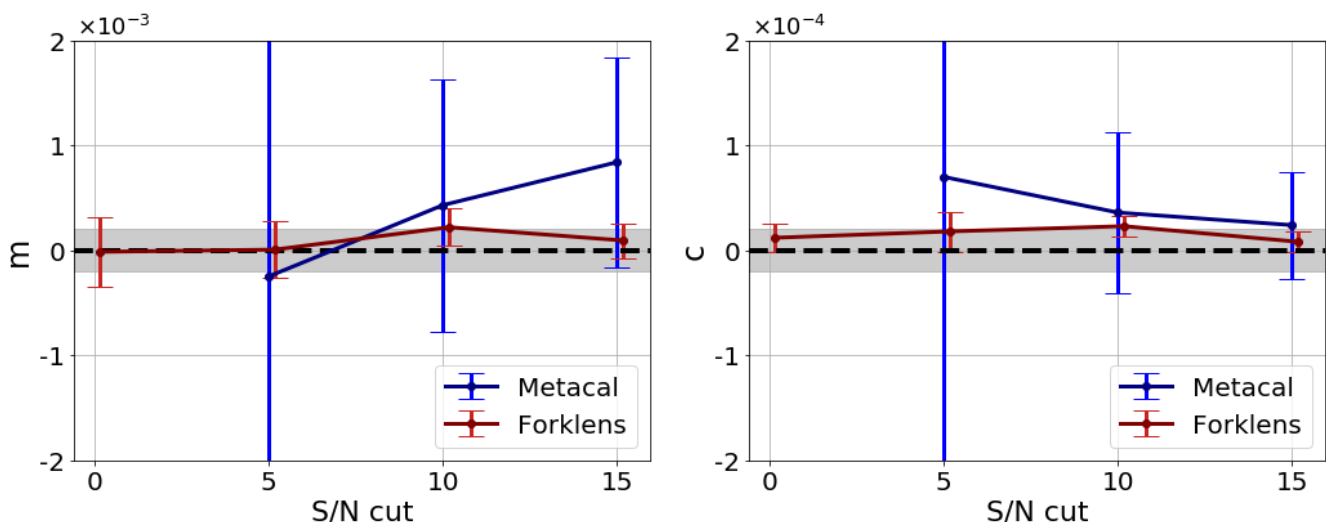


Fig. 11. Shear measurement bias m (top panel) and c (bottom panel) of METACALIBRATION and FORKLENS on CSST simulation as a function of data minimum S/N. Grey regions are the requirement for stage IV weak lensing experiments, 2×10^{-3} and 2×10^{-4} for m and c respectively. METACALIBRATION requires an S/N cut at a minimum of 5 to get reliable results, while our approach works well with all samples included. The FORKLENS method also demonstrates much tighter scattering than METACALIBRATION, which corresponds to the strength of CNN on faint objects compared to model fitting.

narios for future tests. Secondly, the data we used in analyzing is perfectly consistent with the simulation we used in training (although they are different). We expect our simulation well emulate the real observation, which is not always the case. We shall consider various effects and explore the sensitivity of DL-based methods to them in the following works.

4.4. Time consumption

As one of the general advantages for nearly all ML methods, CNN measurement is high-speed. With two parallel GPUs and 40 CPU threads (one GPU sees no significant decrease in speed), our CNN takes ~ 0.6 milliseconds per galaxy measurement. The time consumption of NN calibration is negligible, ~ 24 seconds on 10 million galaxies with 8 networks each in one thread. In comparison, according to our test, METACALIBRATION together with model fitting takes ~ 6 milliseconds per galaxy in 40 threads.

Training the models also requires time. It took ~ 8 hours to reach the optimized model of CNN, with one GPU and 8 threads. For NN, the accuracy reaches convergence in ~ 15 hours for 8 independent networks simultaneously. Time consumption for training is comparable to that of practical measurements, although once the model is trained following measurement will be fast. A larger volume of training data will also reduce the time for the model to converge.

5. Conclusion and discussion

We introduced a fully DL-based approach FORKLENS to measure galaxy shapes and calibrate weak lensing shear. To handle the effect of PSF smearing on observed galaxy shapes efficiently, we developed a two-branch CNN architecture for involving information of galaxy images and PSF simultaneously. Then, we adopt a multiple-layer neural network to calibrate the shear bias primarily from the pixel noise. Testing the feasibility of our approach with mock data of CSST, FORKLENS achieves negligible bias in shear measurement with $m = -0.4 \pm 3.0 \times 10^{-3}$ and $c = -0.5 \pm 1.9 \times 10^{-4}$. Expectedly, such a setup is suitable

for existing and upcoming weak lensing surveys, including both ground- and space-based experiments such as KiDS, DES, *Euclid*, *Roman*, LSST, etc.

We adopted three approaches to estimate galaxy shapes, which are CNN, moment-based method and forward model fitting. The results present that FORKLENS has the best performance. Specifically, the three methods deliver estimations with similar accuracy on the images with high S/N. However, traditional methods display a rapid drop in accuracy with decreasing S/N and fail to provide reliable measurements when $S/N < 5$, while FORKLENS gives consistent accuracy for both bright and faint objects. A similar trend can also be seen compared with METACALIBRATION. Due to the limitation of the model fitting method, METACALIBRATION usually requires a minimum S/N in the data, while FORKLENS can provide tight shear estimation for galaxies with S/N down to 2. Worth mentioning that, On CSST-like mock images, FORKLENS reaches a part-in-a-thousand accuracy and better with over 50% images of $S/N < 10$.

The whole process of our approach is fully automatic, and it costs 0.6 milliseconds for one galaxy if we ignore the time consumption of training, which is ~ 10 times faster than METACALIBRATION integrated with forward model fitting shape measurement. The time to train the networks dominates the cost, requiring ~ 23 hours to get trained models of CNN and NN. The automation and efficiency of FORKLENS make it possible to handle tens of billions of galaxy images from the upcoming large-scale sky surveys with PB-level data.

One highlighted feature of this work is to include separate information in the inputs, which makes it possible for the network to directly learn various effects (in this case, PSF) affecting the target and output corrected results. Maresca et al. (2021) has adopted a similar fork-like structure with inputs of pixelated source reconstructions and residual images to classify strong lensing source reconstructions and avoid unphysical ones. GALNETS (Li et al. 2022) presents a very similar CNN to FORKLENS. It also takes PSF images as extra-fed information and predicts the Sersic parameters of galaxies. The concept can be easily extrapolated to other possible situations. One potential example is to

use multi-branch CNN to predict galaxy photometric redshift by inputting pixelated images in multiple bands. It might be able to learn all-colour morphology and predict simultaneously various properties useful in weak lensing like shapes and redshifts.

Although CNN requires few prior assumptions, modeling the training set needs to be carefully treated. It is necessary to consider more realistic galaxy profiles in the following works, such as modeling multiple components, including bulges, disks, and knots. At higher redshifts, galaxies also show different morphology from the more recent Universe. In this work, we assume the input PSF is perfectly known. It is also important to know the CNN sensitivity to PSF model bias when it is incorrectly reconstructed. Another potential improvement is implementing the Bayesian Neural Network (BNN) into our model. The BNN's (Denker & LeCun 1990; Perreault Levasseur et al. 2017) parameters are a probability distribution with trainable variances and means instead of fixed weights and biases, which can capture the uncertainties of estimation and provide a confidence level for each output.

To summarize, we have proposed the FORKLENS for measuring weak lensing shears. According to the tests with CSST mock data, FORKLENS provides better estimation and higher efficiency than traditional methods. The idea of multiple input paths can be easily extrapolated to other applications, e.g., multi-colour measurements. Besides, the current model requires further sensitivity analysis. We plan future tests on the robustness of this method in various realistic situations where current results may face challenges.

Acknowledgements. This work is supported by National Key R&D Program of China No. 2022YFF0503403. We also acknowledge the support from the science research grants from the China Manned Space Project with No. CMS-CSST-2021-A01, No. CMS-CSST-2021-A03, No. CMS-CSST-2021-B01 and NSFC of China under grant U1931210. HYS acknowledges the support from NSFC of China under grant 11973070, Key Research Program of Frontier Sciences, CAS, Grant No. ZDBS-LY-7013 and Program of Shanghai Academic/Technology Research Leader. CLW acknowledges the support from NSFC of China under grant 11903082. JY acknowledges the support from NSFC Grant No.12203084. RL acknowledges the support from NSFC Grants (Nos 11988101,12022306), CAS Project for Young Scientists in Basic Research (No. YSBR-062), and the support from K.C.Wong Education Foundation.

References

Aihara, H., Armstrong, R., Bickerton, S., et al. 2018, PASJ, 70, S8
 Bacon, D. J., Refregier, A. R., & Ellis, R. S. 2000, MNRAS, 318, 625
 Bernstein, G. M. & Armstrong, R. 2014, MNRAS, 438, 1880
 Bernstein, G. M., Armstrong, R., Krawiec, C., & March, M. C. 2016, MNRAS, 459, 4467
 Bernstein, G. M. & Jarvis, M. 2002, AJ, 123, 583
 Denker, J. S. & LeCun, Y. 1990, in Proceedings of the 3rd International Conference on Neural Information Processing Systems, NIPS'90 (San Francisco, CA, USA: Morgan Kaufmann Publishers Inc.), 853–859
 Fenech Conti, I., Herbonnet, R., Hoekstra, H., et al. 2017, MNRAS, 467, 1627
 Fluri, J., Kacprzak, T., Refregier, A., et al. 2018, Phys. Rev. D, 98, 123518
 Gruen, D., Seitz, S., Koppenhoefer, J., & Riffeser, A. 2010, ApJ, 720, 639
 Guinot, A., Kilbinger, M., Farrens, S., et al. 2022, A&A, 666, A162
 Han, Y., Zou, Z., Li, N., & Chen, Y. 2022, Research in Astronomy and Astrophysics, 22, 085006
 He, K., Zhang, X., Ren, S., & Sun, J. 2015, arXiv e-prints, arXiv:1512.03385
 Heymans, C., Van Waerbeke, L., Bacon, D., et al. 2006, MNRAS, 368, 1323
 Hildebrandt, H., Viola, M., Heymans, C., et al. 2017a, MNRAS, 465, 1454
 Hildebrandt, H., Viola, M., Heymans, C., et al. 2017b, MNRAS, 465, 1454
 Hirata, C. & Seljak, U. 2003, MNRAS, 343, 459
 Hoekstra, H., Herbonnet, R., Muzzin, A., et al. 2015, MNRAS, 449, 685
 Huff, E. & Mandelbaum, R. 2017, arXiv e-prints, arXiv:1702.02600
 Jarvis, M., Sheldon, E., Zuntz, J., et al. 2016, MNRAS, 460, 2245
 Jeffrey, N., Lanusse, F., Lahav, O., & Starck, J.-L. 2020, MNRAS, 492, 5023
 Kaiser, N. 2000, ApJ, 537, 555
 Kaiser, N., Squires, G., & Broadhurst, T. 1995, ApJ, 449, 460
 Krause, E., Eifler, T. F., Zuntz, J., et al. 2017, arXiv e-prints, arXiv:1706.09359

Krizhevsky, A., Sutskever, I., & Hinton, G. E. 2012, in Advances in Neural Information Processing Systems, ed. F. Pereira, C. Burges, L. Bottou, & K. Weinberger, Vol. 25 (Curran Associates, Inc.)
 Kuijken, K., Heymans, C., Hildebrandt, H., et al. 2015, MNRAS, 454, 3500
 Lanusse, F., Mandelbaum, R., Ravanbakhsh, S., et al. 2021, MNRAS, 504, 5543
 Lathuilière, S., Mesejo, P., Alameda-Pineda, X., & Haud, R. 2020, IEEE Transactions on Pattern Analysis and Machine Intelligence, 42, 2065
 Laureijs, R., Amiaux, J., Arduini, S., et al. 2011, arXiv e-prints, arXiv:1110.3193
 Li, H. & Zhang, J. 2021, ApJ, 911, 115
 Li, R., Napolitano, N. R., Roy, N., et al. 2022, ApJ, 929, 152
 Li, X., Li, Y., & Massey, R. 2022, Monthly Notices of the Royal Astronomical Society, 511, 4850
 Li, X. & Mandelbaum, R. 2022, arXiv e-prints, arXiv:2208.10522
 LSST Science Collaboration, Abell, P. A., Allison, J., et al. 2009, arXiv e-prints, arXiv:0912.0201
 Lu, T., Haiman, Z., & Zorrilla Matilla, J. M. 2022, MNRAS, 511, 1518
 MacCrann, N., Becker, M. R., McCullough, J., et al. 2022, MNRAS, 509, 3371
 Mandelbaum, R. 2018, ARA&A, 56, 393
 Mandelbaum, R., Rowe, B., Bosch, J., et al. 2014, ApJS, 212, 5
 Maresca, J., Dye, S., & Li, N. 2021, MNRAS, 503, 2229
 Massey, R., Hoekstra, H., Kitching, T., et al. 2013, MNRAS, 429, 661
 Massey, R. & Refregier, A. 2005, MNRAS, 363, 197
 Massey, R., Rowe, B., Refregier, A., Bacon, D. J., & Bergé, J. 2007, MNRAS, 380, 229
 Melchior, P. & Viola, M. 2012, MNRAS, 424, 2757
 Melchior, P., Viola, M., Schäfer, B. M., & Bartelmann, M. 2011, MNRAS, 412, 1552
 Miller, L., Heymans, C., Kitching, T. D., et al. 2013, MNRAS, 429, 2858
 Nakajima, R. & Bernstein, G. 2007, AJ, 133, 1763
 Nurbaeva, G., Tewes, M., Courbin, F., & Meylan, G. 2015, A&A, 577, A104
 Paulin-Henriksson, S., Amara, A., Voigt, L., Refregier, A., & Bridle, S. L. 2008, A&A, 484, 67
 Paulin-Henriksson, S., Refregier, A., & Amara, A. 2009, A&A, 500, 647
 Pearson, J., Li, N., & Dye, S. 2019, MNRAS, 488, 991
 Pearson, J., Maresca, J., Li, N., & Dye, S. 2021, MNRAS, 505, 4362
 Perreault Levasseur, L., Hezaveh, Y. D., & Wechsler, R. H. 2017, ApJ, 850, L7
 Pujol, A., Bobin, J., Sureau, F., Guinot, A., & Kilbinger, M. 2020, A&A, 643, A158
 Rhodes, J., Refregier, A., & Groth, E. J. 2000, ApJ, 536, 79
 Ribli, D., Dobos, L., & Csabai, I. 2019a, MNRAS, 489, 4847
 Ribli, D., Pataki, B. Á., & Csabai, I. 2019b, Nature Astronomy, 3, 93
 Rowe, B. T. P., Jarvis, M., Mandelbaum, R., et al. 2015, Astronomy and Computing, 10, 121
 Sheldon, E. 2015, NGMIX: Gaussian mixture models for 2D images, Astrophysics Source Code Library, record ascl:1508.008
 Sheldon, E. S., Becker, M. R., MacCrann, N., & Jarvis, M. 2020, ApJ, 902, 138
 Sheldon, E. S. & Huff, E. M. 2017, ApJ, 841, 24
 Shirasaki, M., Yoshida, N., & Ikeda, S. 2019, Phys. Rev. D, 100, 043527
 Spergel, D., Gehrels, N., Baltay, C., et al. 2015, arXiv e-prints, arXiv:1503.03757
 Springer, O. M., Ofek, E. O., Weiss, Y., & Merten, J. 2020, MNRAS, 491, 5301
 Tewes, M., Kuntzer, T., Nakajima, R., et al. 2019, A&A, 621, A36
 Viola, M., Kitching, T. D., & Joachimi, B. 2014, MNRAS, 439, 1909
 Wei, S., Li, Y., Lu, W., et al. 2022, PASP, 134, 114508
 Yamamoto, M., Troxel, M. A., Jarvis, M., et al. 2022, MNRAS[arXiv:2203.08845]
 Zeiler, M. D. & Fergus, R. 2014, in Computer Vision – ECCV 2014, ed. D. Fleet, T. Pajdla, B. Schiele, & T. Tuytelaars (Cham: Springer International Publishing), 818–833
 Zhan, H. 2011, Sci. China-Phys. Mech. Astron., 41(12), 1441
 Zhan, H. 2021, Sci. Bull., 66, 1290
 Zhang, J., Dong, F., Li, H., et al. 2019, ApJ, 875, 48
 Zuntz, J., Sheldon, E., Samuroff, S., et al. 2018, MNRAS, 481, 1149